Available online at www.sciencedirect.com
ScienceDirect
Trans. Nonferrous Met. Soc. China 32(2022) 1428−1441
Transactions of Nonferrous Metals Society of China
www.tnmsc.cn

Strong and ductile Al−Zn−Mg−Zr alloy obtained by equal angular pressing and subsequent aging

Lei TANG[1], Xiao-yan PENG[2,3], Fu-qing JIANG[4], Yao LI[2], Guo-fu XU[2,3]

1. School of Metallurgy and Materials, University of Birmingham, B15 2TT, United Kingdom;
2. School of Materials Science and Engineering, Central South University, Changsha 410083, China;
3. Key Laboratory of Nonferrous Metallic Materials Science and Engineering, Ministry of Education, Central South University, Changsha 410083, China;
4. Institute of Metal Research, Chinese Academy of Sciences, Shenyang 110016, China

Received 6 January 2022; accepted 30 March 2022

Abstract: An ultrafine-grained Al−Zn−Mg−Zr alloy with superior mechanical performance was obtained by high passes of equal angular pressing (ECAP) and subsequent aging. After 8 ECAP passes and aging, the yield strength (YS) and ultimate tensile strength (UTS) of the solid-solutioned alloy are significantly improved from (98±10) and (226±7) MPa to (405±9) and (427±9) MPa, respectively. A large elongation is also maintained ((17.4±2.5)%). The microstructure features including grain refinement, morphology of precipitates, and dislocation density, were revealed with multiscale characterizations, including transmission electron microscopy, electron backscattered diffraction, and X-ray diffraction. After 8 passes of ECAP, the original coarse elongated grains are refined to a unique bimodal grain structure consisting of ultrafine equiaxed and lath-like grains. Additionally, the effects of ECAP and subsequent aging on the strengthening contribution of a variety of strengthening mechanisms, such as dislocation strengthening and precipitation strengthening, were discussed in detail.

Key words: equal angular pressing; Al−Zn−Mg−Zr alloy; grain refinement; strengthening mechanism

1 Introduction

Serving as a workhorse structural material with light weight, desirable mechanical performance, and excellent resistance to oxidation and corrosion, aluminum alloys have been receiving huge research interest and playing an critical role in multiple applications [1−7]. Many methods (e.g., micro-alloying with Mn [8], Si, and Cu [6]) were developed to obtain premier comprehensive mechanical performance. However, the addition of these transition elements can lead to the element segregation and formation of intermetallics, such as the Mg-rich phase [9] and Cu-rich phase [10], which can not only induce stress concentration at phase−matrix interfaces but also lead to the deterioration of ductility and resistance to corrosion.

Over the last two decades, the combination of heat-treatable aluminum alloys with severe plastic deformation (SPD), has emerged and attracted huge research interest due to its ability of introducing multiple strengthening mechanisms, such as precipitation strengthening, dislocation strengthening, and fine grain strengthening. It is a very promising method in achieving superior strength−ductility combinations without changing the chemical composition [11−14]. Compared with other SPD methods (e.g., high-pressure torsion [15] and accumulative roll bonding [16]), equal angular pressing (ECAP) [17,18] has shown great

Corresponding author: Guo-fu XU, Tel/Fax: +86-731-88877217, E-mail: csuxgf66@csu.edu.cn
DOI: 10.1016/S1003-6326(22)65884-9
1003-6326/© 2022 The Nonferrous Metals Society of China. Published by Elsevier Ltd & Science Press

advantages in processing bulk materials and providing significant strengthening effects via refining grain size to the sub-micrometer (100−1000 μm) or even nanometer (<100 nm) range. ZHA et al [19] reported that ECAP can introduce high density of dislocation barriers to an Al−7Mg alloy, and the yield strength (YS) was more than tripled from ~133 to ~446 MPa after 3 ECAP passes at room temperature. Similarly, an ultrafine-grained structure of a 7075 alloy (with an averaged width of (150±20) nm and length of (430±30) nm) was obtained after 2 ECAP passes, more than doubling the YS from 320 to 650 MPa [20].

Even with promising strengthening effects, there are very few studies focusing on processing heat-treatable aluminum alloys with high ECAP passes (>4) at room temperature due to the high risk of causing severe damage to ECAP die and samples. The evolution of microstructure (e.g., grain refinement procedure and dislocation activity) and the corresponding strengthening effects during ECAP and after subsequent aging have rarely been investigated. Herein, to build a comprehensive understanding of the effects of high-pass ECAP and post-deformation aging treatment on the mechanical performance and strengthening effects of an Al−Zn−Mg−Zr alloy, a hot extruded 7003 aluminum alloy was processed with different ECAP passes (from 0 to 12) at room temperature and following aging treatment. The mechanical performance was evaluated with tensile tests, while the evolution of microstructure was revealed by multiscale microscopic characterizations, such as X-ray diffraction, transmission electron microscopy (TEM), and electron backscattered diffraction (EBSD). Furthermore, the strength contributions from a variety of hardening mechanisms, such as dislocation strengthening, grain boundary hardening, and precipitation hardening, were discussed and compared with the experimental results. This study provides an in-depth micro-mechanical understanding of the excellent mechanical performance obtained by high passes of ECAP and following aging, paving a way in achieving superior strength−ductility combinations via activating a variety of strengthening mechanisms.

2 Experimental

2.1 Materials preparation

A commercial hot extruded 7003 aluminum alloy was prepared for raw material in the present study. The chemical composition of the alloy is given in Table 1. The hot extruded material was machined into cylinder bars with a diameter of 10 mm and a length of 70 mm. The ECAP process was carried out with a vertical hydraulic press at a pressing speed of 5 mm/s. To protect the ECAP die and avoid sample fracture, the samples were then performed with different ECAP passes (0−12) immediately after a solution treatment at 475 °C for 1 h and water quenching. Meanwhile, a mixture of MoS_2 and graphite was used as a lubricant to reduce the friction between the die and sample. The schematical illustration of the ECAP die is shown in Fig. 1(a). Between the two pressing channels, the intersection angle of 110° and the outer arc angle of 30° create the shear zone, where the large shear strain was imposed on the alloy. The pressing strategy of Bc route was illustrated in Fig. 1(b), which means that the bars were rotated 90° along the pressing direction in the same sense after each ECAP pass. As shown in Fig. 1(c), the samples can maintain a smooth surface even after 8 ECAP passes, while the two sides of the samples were damaged during extrusion. The samples subjected to 0 and 8 ECAP passes were then aged at 120 °C for 12 h.

Table 1 Chemical composition of 7003 aluminum alloy (wt.%)

Zn	Mg	Cu	Mn	Zr	Al
6.0	0.7	0.20	0.12	0.15	Bal.

2.2 Tensile tests

The dog-bone-shaped tensile test samples (15 mm × 6 mm × 2 mm, with a gauge length of 4 mm) were machined at the center of each bar along the extrusion direction (ED) based on GB/T 228—2002. The tensile tests were performed at room temperature on an electronic universal testing machine (MTS−810) equipped with a laser extensometer (LX500) with a strain rate of 0.001 s^{-1}.

2.3 Microstructure characterization

The dislocation density calculation was based on the X-ray diffraction (XRD), which was performed on a high-resolution X-ray diffractometer (Rigaku SmartLab) operating at 40 kV and 30 mA. The Cu K_α radiation including $K_{\alpha1}$ (with a

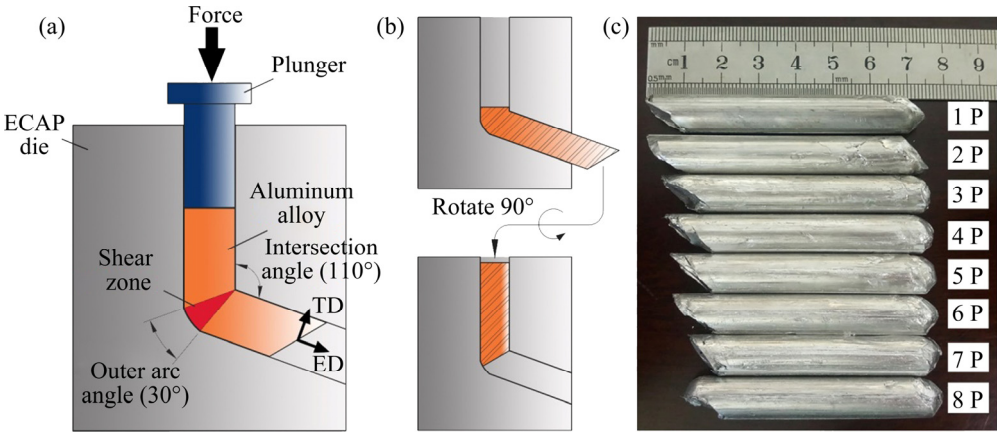

Fig. 1 Schematic illustration of geometry of ECAP die (a), Bc pressing route (b), and photo of samples after different passes of ECAP (c) (ED and TD denote the extrusion and transverse directions, respectively)

wavelength of 1.54056 Å) and $K_{\alpha 2}$ (with a wavelength of 1.54439 Å) was produced, and the diffraction signal was collected from 10° to 90° with a scanning speed of 1 (°)/min, and a step size of 0.02°.

Samples for TEM and EBSD characterization were mechanically polished to a thickness of ~80 μm and then prepared by twin-jet electro-polishing at a voltage of 20 V in a solution consisting of 30% nitric acid and 70% methanol cooled down to −30 °C. TEM observation was performed on an FEI Tecnai F20 TEM with an accelerate voltage of 200 kV. The high-resolution EBSD was carried out on an FEI Sirion 200 field emission gun scanning electron microscope (SEM) with an operating voltage of 20 kV and a step size of 0.03 μm. The collected EBSD data were then analyzed with the OIM 5.3 software. Misorientation less than 2° was ignored to avoid ambiguity. The low angle grain boundaries (LAGBs) were then defined as the boundaries with misorientation angles in the range of 2°−15°, while the misorientation higher than 15° was designated as high angle grain boundaries (HAGBs). The average grain size was determined with the mean linear intercept method.

3 Results and discussion

3.1 Original microstructure

Figure 2 reveals the original microstructure of the hot extruded 7003 aluminum alloy before ECAP. The index coefficient (IC) map (Fig. 2(a)) shows that the microstructure of the hot extruded sample mainly consists of coarse elongated grains with dimensions >500 μm and ~20 μm along ED and TD, respectively. Meanwhile, some small (sub)-grains (with a grain size ~2 μm) distributing around large grains are also observed. The typical inverse pole figure (IPF) of Fig. 2(a) overlapped with grain boundaries (LAGBs: red lines and HAGBs: black lines) is shown in Fig. 2(b), where the color of each point was based on its orientation. The [001] inverse pole figure is shown in the corner of Fig. 2(b). A low density of LAGBs is also observed in the grain interior, separating the large and elongated grains into several smaller subgrains. In Fig. 2(c), the misorientation distribution of the extruded sample is compared with the random misorientation distribution. The LAGBs of the extruded sample have a very high fraction of 68.9% compared with the HAGBs of only 31.1%. The microstructure is further revealed by the bright-field TEM image shown in Fig. 2(d). Small equiaxed grains with a diameter of several micrometers are observed. However, in the grain interiors, even the dislocation density is low, some dislocation entanglements can still be observed. The formation of the fine equiaxed grains around the large grains can be ascribed to the recrystallization resulted from the high stress concentration along the grain boundaries and high temperature during the hot extrusion [21]. This process can also induce rapid dislocation annihilation and reduce the dislocation density [22]. In addition, the microstructure of the hot extruded sample is almost unchanged during the following solid solution treatment.

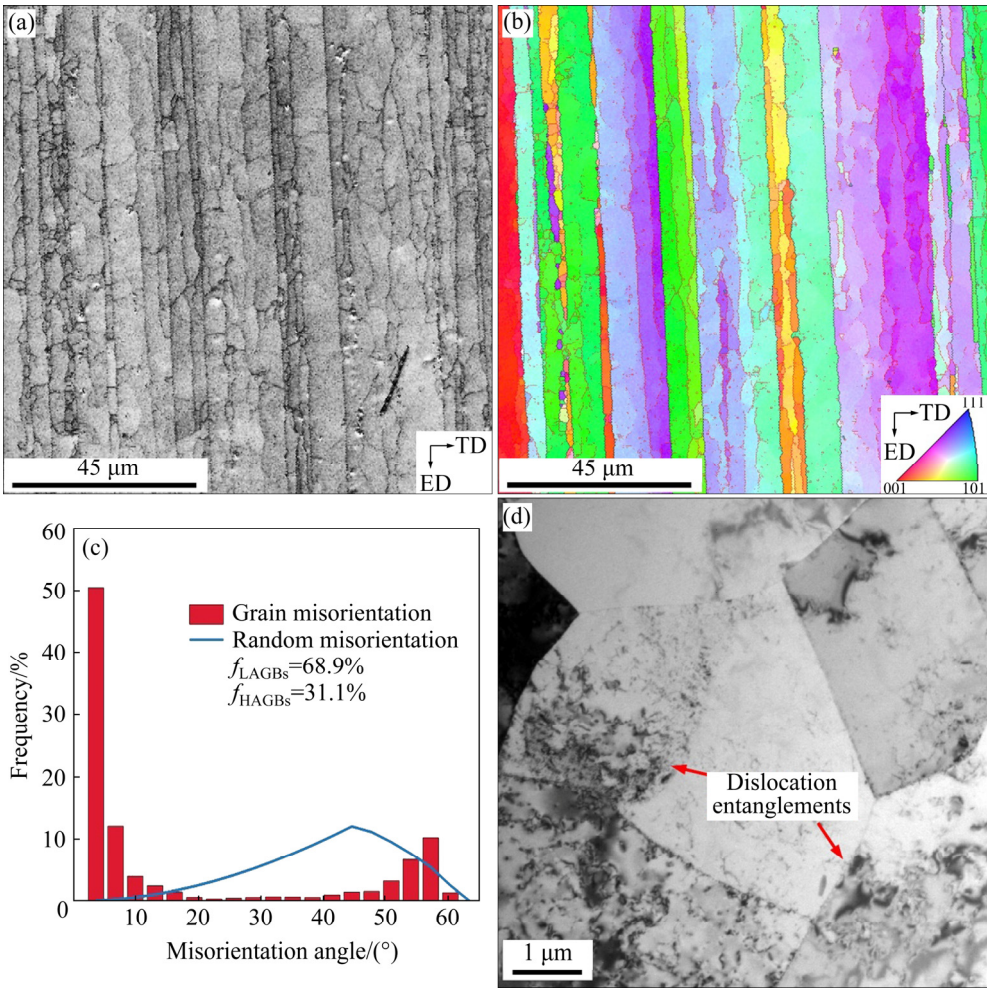

Fig. 2 Microstructure characteristics of as-extruded alloy: (a) IC (index coefficient) map; (b) Typical inverse pole figure (IPF); (c) Comparison between misorientation distribution of sample and random misorientation; (d) Typical bright-field TEM image

3.2 Mechanical performance

Engineering stress−strain curves of the alloy processed with different ECAP passes and aging are shown in Fig. 3(a). Before ECAP, the sample (0 P) is very soft and ductile as it shows a very low YS of (98±10) MPa, ultimate tensile strength (UTS) of (226±7) MPa, and elongation of (24.7±1.9)% due to the reduced dislocation density. After a single ECAP, the YS and UTS are then significantly improved to (275±9) and (312±9) MPa, respectively, while the elongation is decreased to (19.3±2.3)%. The YS and UTS of the alloy can be progressively improved with the increase of ECAP pass while the elongation also maintains at a high level of ~15%. The premier mechanical performance is achieved after 8 ECAP passes with YS of (390±7) MPa, UTS of (430±5) MPa, and elongation of (16.0±2.2)%. After aging, the YS of the 8 P sample is further improved to (405±9) MPa with UTS maintaining at a high level of (427±9) MPa. Its elongation is also increased to (17.4±2.5)%. However, the strength enhancement brought by ECAP is not unlimited: after 12 ECAP passes, the YS and UTS are reduced to (375±10) and (406±9) MPa, respectively, and the elongation is also decreased to (12.6±1.9)%. The mechanical performance deterioration occurring in the 12 P sample may be ascribed to the formation of microcracks after extremely large shear deformation. The mechanical properties of the alloy processed with different ECAP passes and subsequent aging are summarized in Fig. 3(b) and listed in Table 2.

3.3 Microstructure after ECAP and aging

The microstructure of the alloy subjected to low ECAP passes (1 and 2) is revealed by EBSD

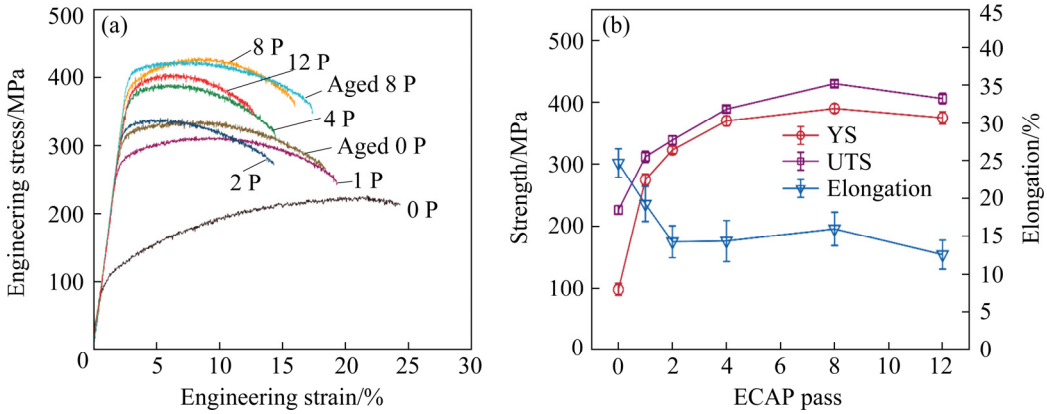

Fig. 3 Mechanical performance of alloy processed with different ECAP passes and heat treatment: (a) Engineering stress−strain curves; (b) Mechanical properties plotted as function of ECAP pass

Table 2 Mechanical properties of alloy processed with different ECAP passes and following aging

Sample	YS/MPa	UTS/MPa	Elongation/%
0 P	98±10	226±7	24.7±1.9
Aged 0 P	311±5	336±8	18.4±1.5
1 P	275±9	312±9	19.3±2.3
2 P	323±6	339±7	14.3±2.1
4 P	370±8	389±5	14.4±2.7
8 P	390±7	430±5	16.0±2.2
Aged 8 P	405±9	427±9	17.4±2.5
12 P	375±10	406±9	12.6±1.9

maps shown in Fig. 4. Figures 4(a, b) show the typical IPF map and corresponding IC map of the alloy after a single ECAP pass, respectively. Massive parallel micro shear bands are produced along almost 45° to the ED. The original coarse and elongated grains are then separated into several refined subgrains by these micro shear bands. Compared with the sample before ECAP (Fig. 2(b)), the density of LAGBs is significantly increased in grain interiors, indicating the very active dislocation multiplication and interaction. After 2 ECAP passes, the alloy shows a uniform deformation behavior. As revealed by the IPF and IC map (Figs. 4(c, d), respectively), a macro shear band with a width of ~120 μm is produced, consisting of very dense intersecting micro shear band networks and LAGBs (Fig. 4(d)). The original coarse elongated grains are then refined into small equiaxed grains (~4 μm) (Fig. 4(c)). Outside the macro shear band, the microstructure is very similar to that of the 1 P sample. This indicates that the plastic deformation

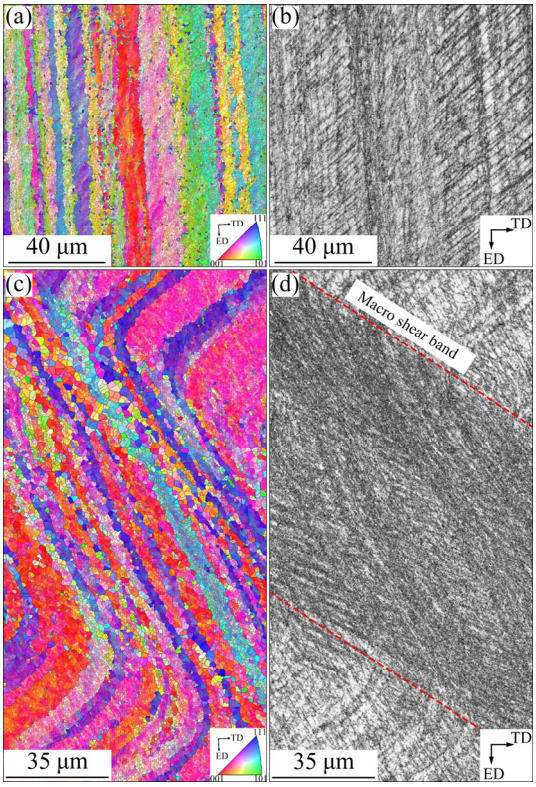

Fig. 4 Typical IPF maps (a, c) and IC (index coefficient) maps (b, d) showing microstructure of sample processed with 1 pass (a, b) and 2 passes (c, d)

can be mainly withstood by the macro shear bands. The formation of shear bands is discontinuous, and this may be originated from the high strain rate. When the alloy is pressed into the shear zone, the inhomogeneities of the alloy can lead to some concentration areas of plastic deformation. The high strain rate can generate more heat than the dissipated heat and raise temperature of these areas [23]. Higher local temperature leads to softening effects and more deformation in these

areas [24]. These areas then become shear bands and cater higher plastic deformation.

The grain morphology of the sample subjected to high ECAP passes is shown in Fig. 5. As shown in Fig. 5(a), after 4 ECAP passes, the microstructure mainly consists of large grains (~5 μm) surrounded by ultrafine grains with a diameter less than 1 μm, indicating the significant grain refinement after repetitive ECAP processing. After 8 ECAP passes, the grains are further refined, and almost all coarse grains are transferred into ultrafine equiaxed grains with an average grain size of 0.77 μm (Fig. 5(b)).

To further reveal the grain refinement procedure of ECAP, TEM images of samples processed with different ECAP passes are shown in Figs. 6 and 7. Figures 6(a, b) show the typical bright-field TEM images of the alloy subjected to a single ECAP pass. The large shear strain significantly enhances the dislocation density as very dense dislocation entanglements can be observed in Fig. 6(a), where some thin and lath-like grains (with a width of ~200 nm and length >1 μm) are produced. The high dislocation density induces very large residual stress, and many fuzzy grain boundaries can be frequently observed and can be identified as Moiré patterns [19]. The grain interior shows much lower dislocation density than the boundaries of substructures since dislocations can be absorbed by LAGBs or form additional HAGBs, dislocation walls, or polygonized dislocation walls directly (Fig. 6(b)). These substructures can significantly refine the original coarse grains, which can provide effective barriers for dislocation motions thus providing strengthening effects [19]. Meanwhile, the precipitation of Al_3Zr dispersoids with $L1_2$ structure can be observed in the dark-field TEM image shown in Fig. 6(c). These particles distribute homogeneously among the Al matrix with an average diameter of ~22 nm. The morphology of the Al_3Zr dispersoid and the coherent interface between Al_3Zr particles and Al matrix are further revealed by the high-resolution TEM (HRTEM) image shown in Fig. 6(d). Similar precipitation behavior can also be found in Ref. [25]. After 2 ECAP passes, more lath-like grains and dislocation entanglements are produced (Fig. 6(c)). The unique ECAP route (Bc) can create intersecting of shear planes, thus imposing rotating direction of shear strain to the sample. Many new shear bands are created by activating additional slip systems after the second ECAP pass. It can not only soar the dislocation density but also collide over the preexisting shear bands, thus further refining the grain structure (Fig. 6(f)).

As shown in Fig. 7(a), after 4 ECAP passes, many coarse grains are further refined into many equiaxed grains (with diameter <1 μm). The repetitive shear deformation significantly induces the possibility of the collision of shear bands and produces higher dislocation density. The high dislocation clusters progressively form LAGBs and gradually transfer into fuzzy grain boundaries (Fig. 7(b)). The formed cell structures show a smaller size (~200 nm in width and ~500 nm in length) than those with low ECAP passes (Fig. 6(b)). Due to the large strain, dynamic recrystallization occurs even at room temperature as ultrafine equiaxed recrystallized grains (~300 nm) can also

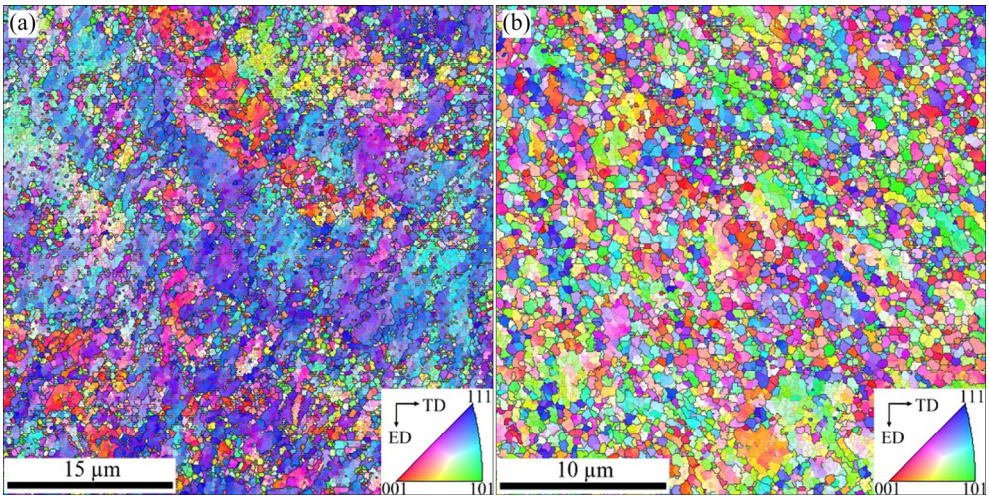

Fig. 5 Typical IPF maps showing grain morphology of alloy subjected to different ECAP passes: (a) 4 passes; (b) 8 passes

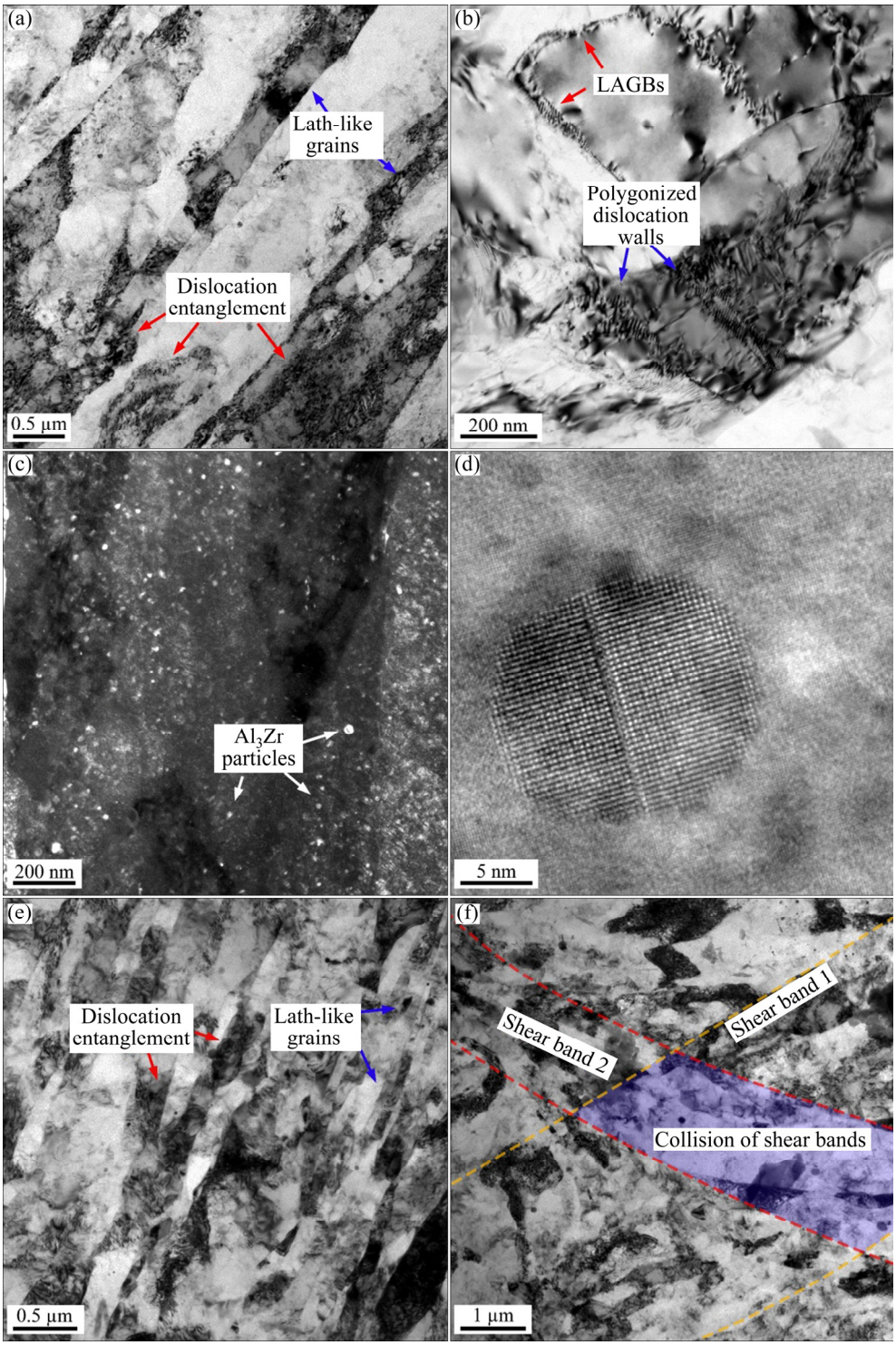

Fig. 6 Microstructures of alloy processed with low ECAP passes: (a−d) 1 pass; (e, f) 2 passes

be observed (Fig. 7(b)). As the ECAP pass is increased to 8, the alloy shows an ultrafine-grained structure consisting of short lath-like grains and ultrafine equiaxed grains (Fig. 7(c)). The fraction of ultrafine recrystallized grains is increased significantly (Fig. 7(d)).

Based on the microscopy observation, three types of refined grains can be observed after repetitive passes of ECAP: long lath-like grains, short lath-like grains, and ultra-fine equiaxed grains. Three different procedures can be involved during the grain refinement. (1) At low ECAP passes (N=1, 2), the dislocations and formation of shear bands can be the main strain carrier. The highly active

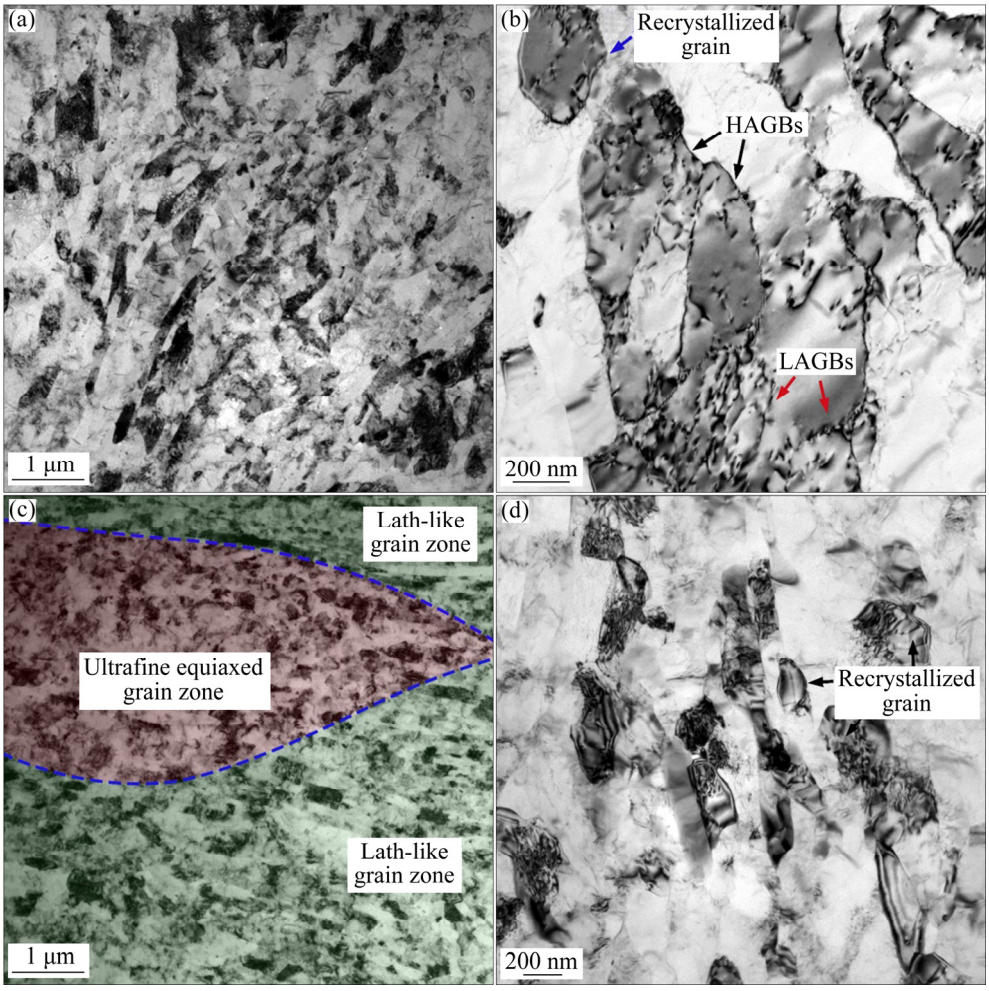

Fig. 7 Typical bright-field TEM images of alloy subjected to high ECAP passes: (a, b) 4 passes; (c, d) 8 passes

dislocation motion along the slip planes can produce massive parallel shear bands. With the increase of strain, the gathered dislocations can further transform into massive parallel grain boundaries, slicing the original grains into many long lath-like grains (with a width of ~200 nm and length >1 μm). (2) During ECAP, the high dislocation density is also created in grain interiors (Fig. 6). These dislocations can produce dislocation entanglements and form LAGBs at low ECAP passes. With the increase of strain, higher dislocation density is observed and the LAGBs gradually transfer into HAGBs, cutting the long lath-like grains into even finer lath-like grains (with a width of ~200 nm and thickness of ~800 nm, Fig. 7(c)). A similar grain refinement procedure was also reported in Ref. [20] after imposing an equivalent strain of ~2. (3) The collision of shear bands can be very frequent due to the large and multidirectional shear strain brought by repetitive ECAP. The ultrafine equiaxed grains (with diameter <500 nm) can be formed at the intersection of shear bands, where different slip systems are activated, and the possibility of forming/trapping dislocations is significantly enhanced.

The dislocation motions (e.g., multiplication and annihilation) serve as a critical procedure in forming a dense network of dislocation barriers and further refining grains. Herein, the dislocation density of the alloy after different ECAP passes and aging (only with the 8 P sample) is calculated. The X-ray diffraction patterns are applied to calculating the dislocation density with the modified Williamson−Hall method developed by UNGÁR and BORBÉLY [26]:

$$\Delta K \cong \frac{a_s}{D} + bM_d\sqrt{\frac{\pi}{2}}\rho(K\overline{C}_{hkl}^{1/2}) + O\left(K^2\overline{C}\right) \quad (1)$$

where M_d is the dislocation arrangement parameter, a_s/D represents the peak broadening effects caused

by the size effect, a_s (=0.9) is the shape factor for cubic symmetric spherical crystals [27], and D is the crystalline size. b is the magnitude of Burger's vector, $\Delta K=\cos\theta\cdot\beta/\lambda$, β is the full width at half maximum (FWHM) of the diffraction peak, and λ is the wavelength of the incident X-ray. K (=2sin θ/λ) is the modulus of the diffraction vector. $K^2\overline{C}$ is the derivation related to dislocation correction and ignored for simplicity, and $\overline{C}_{hkl}$ is the hkl-dependent average contrast factor [27]. In addition, the peak broadening effect caused by instruments is subtracted with a calibration curve obtained by measuring a standard reference sample (high purity annealed Silicon) [28]. More detailed calculation procedure can be found in Ref. [21].

Figure 8(a) shows the modified Williamson−Hall plots of the sample after different ECAP and aging, where ΔK is plotted and linearly fitted as a function of $K\overline{C}^{0.5}$. The obtained dislocation density evolution with ECAP pass is shown in Fig. 8(b). Before ECAP, the 0 P sample shows a very low dislocation density of ~1.1×10^{13} m^{-2} due to the solid solution treatment. However, after one ECAP pass, the dislocation density soars to 1.73×10^{14} m^{-2}. The following ECAP passes can further increase the dislocation density but at a slower pace. The dislocation density of the 4 P sample is increased to ~4.62×10^{14} m^{-2} which is only increased slightly to ~5.80×10^{14} m^{-2} for the 8 P sample. This indicates that the ability of ECAP in enhancing dislocation density is limited by the recrystallization and dislocation annihilation that occur at high ECAP passes [19,20]. After aging, the dislocation density of the 8 P sample is decreased to ~1.32×10^{14} m^{-2} due to the dislocation annihilation and recovery [29]. The measured dislocation density of the ECAPed samples shows a slightly lower level than that of an Al−7Mg reported in Ref. [19], which reached (5−10)$\times10^{14}$ m^{-2} after 3 ECAP passes. This can be ascribed to the difference in the design of the ECAP die. According to the Iwahashi equation [30], the pressing die angle used in Ref. [19] is 90°, and a very high equivalent strain of ~1.1 is imposed after each ECAP pass. However, this value is decreased to 0.74 due to the 110° intersection angle used in the present study [22].

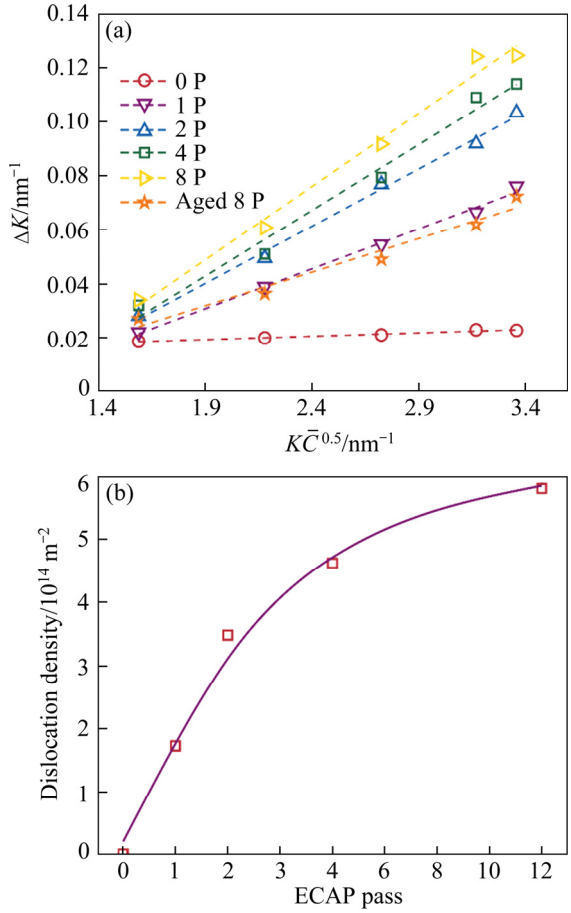

Fig. 8 Modified Williamson−Hall plots of alloy after different treatments (a) and calculated dislocation density evolution as function of ECAP pass (b)

Figure 9(a) shows the IPF map of the 8 P sample after aging treatment. The grain size is slightly increased from ~0.77 to ~1.70 μm. This can be originated from the promoted dislocation annihilation and recovery due to the external thermal activation. Meanwhile, some ultrafine grains can merge and grow into large grains. Figures 9(b, c) show the dark-field TEM image and the HRTEM image of the precipitates of aged 8 P sample, respectively. According to Refs. [31,32], the Al−Zn−Mg alloys with low Mg content follow a precipitation sequence of solid solution → GP zones (GP I and GP II) → η' phase → η phase ($MgZn_2$). The precipitates in the present study show a rod-like shape and distribute evenly among the Al matrix. Their microstructure (with a width of ~2 nm and length of ~3 nm) further revealed by HRTEM is shown in Fig. 9(b). According to Ref. [33], these precipitates can be identified as η' precipitates since multiple ECAP passes can only change the kinetics of the precipitation, without altering its sequence [34]. The morphology, chemical composition, distribution of the η' precipitates are very similar to other 7xxx series aluminum alloys processed with other deformation methods and aging treatment [13,35].

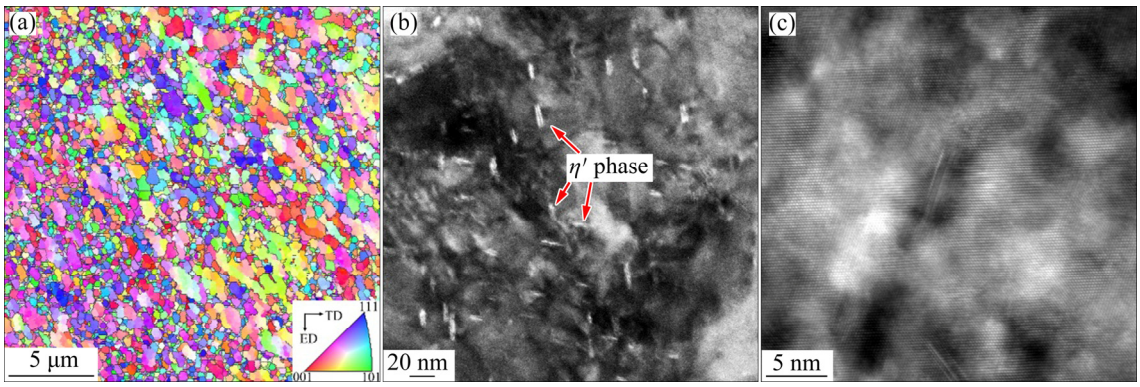

Fig. 9 Microstructure and distribution of precipitates of alloy after 8 ECAP passes and aging: (a) IPF map; (b) Dark-field TEM image of η' phases; (c) HRTEM image of η' phases

3.4 Strengthening effects

To analyze the strengthening effects of different strengthening resources in the 8 P and aged 8 P sample, a superimposed formula is applied to modelling the strength of the alloy [36]:

$$\sigma=\sigma_0+\sigma_{SS}+\sigma_{GB}+\sigma_{dis}+\sigma_P \quad (2)$$

It consists of lattice friction stress (σ_0), solid solution strengthening (σ_{SS}), grain boundary strengthening (σ_{GB}), precipitation strengthening (σ_P), and forest strengthening effects brought by dislocations (σ_{dis}).

According to Ref. [37], the lattice friction stress for pure Al is very low (16 MPa). The strengthening effect of solute atoms in Al−Zn−Mg series alloys can be calculated with the Fleischer equation [38]:

$$\sigma_{SS}=MGb\varepsilon_{ss}^{3/2}\sqrt{c} \quad (3)$$

where G (=26 GPa) is the shear modulus [29], M (=3) is the average Taylor factor for tensile deformation, ε_{ss} is the lattice strain, and c is the concentration of elements. With the chemical composition given in Table 1, the solid solution strengthening effect is calculated to be ~23 MPa.

The strengthening contribution from grain boundaries can be calculated with the classical Hall−Petch equation [36]:

$$\sigma_{GB}=k_{HP}d^{-0.5} \quad (4)$$

where k_{HP} (=0.12 MPa·m$^{0.5}$) is Hall−Petch constant form grain boundaries [38] and d is the average grains size. Based on the average grain size measured in EBSD characterization, d values for the 8 P and aged 8 P sample are determined to be ~0.77 and ~1.70 μm, respectively, and the grain boundaries thus have contributions of ~136 and ~92 MPa to the strength, respectively.

The hardening effect from dislocations can be calculated with Taylor equation [39]:

$$\sigma_{dis}=M\alpha Gb\rho^{1/2} \quad (5)$$

where α is a constant for scaling the interaction strength between dislocations and a value of 0.3 is used according to Refs. [19]. With the measured dislocation density (Fig. 8), the dislocations have contributions of ~161 and ~77 MPa to the strength of the 8 P and aged 8 P sample, respectively.

Before the aging treatment, the precipitation strengthening can be ascribed to the homogeneous distribution of Al_3Zr dispersoids, which may involve two particle size-dependent strengthening mechanisms: the shearing mechanism and bypass by dislocation looping mechanism [40]. When the radius of the particles is very small, the dislocation shearing deformation may occur and three mechanisms are postulated to explain this process: (1) the modulus strengthening originated from the mismatch between the shear moduli difference between the particles and Al matrix, (2) the coherency hardening due to the impedance to dislocation motion of strain fields created by the coherent particles, and (3) ordering hardening resulted from the antiphase boundaries [29]. Alternatively, with the increase of particle size/losing coherency with the matrix, the cutting mechanism becomes more difficult and the Orowan mechanism, which is based on dislocation looping/bowing around the precipitates, is more favorable energetically [31,41]. Based on dark-field

TEM observation on Al_3Zr particles, the average particle radius is estimated to be ~22 nm, so the strength contribution of Al_3Zr particles (σ_{Al_3Zr}) can be modeled with the Orowan strengthening mechanism [7]:

$$\sigma_{Al_3Zr} = K_o M (1-\nu)^{-0.5} \left(\frac{Gb}{\pi\lambda}\right) \ln\left(\frac{\langle r\rangle}{b}\right) \quad (6)$$

where K_o is a particle size-dependent constant, and a value of 0.127 is used according to Ref. [42]; ν(=0.34) is the Poisson's ratio of Al [43]; $\langle r\rangle$ and λ are the mean particle diameter and inter-particle spacing distance, respectively. λ can be calculated by assuming that the particles are spherically arranged on a cubic grid [42]:

$$\lambda = \langle r\rangle \left(\frac{1}{2}\sqrt{\frac{2\pi}{3f_{vs}}} - 1\right) \quad (7)$$

where f_{vs}(=1×10^{-3}) is the volume fraction of the Al_3Zr particle. Therefore, combining Eqs. (6) and (7) yields the strengthening contribution of Al_3Zr to be ~55 MPa.

For the aged 8 P sample, in addition to the precipitation strengthening effect from Al_3Zr particles, an extra strengthening effect is introduced by the massive ultrafine η' precipitates. The rod-like morphology of the precipitates can affect the number of particles intersecting the slip plane, and thus the shape change from sphere to elongated rods can result in extra strength enhancement ($\sigma_{\eta'}$), which is given by [44]

$$\sigma_{\eta'} = M \cdot A \frac{1}{\delta\sqrt{3}\left(\sqrt{\frac{\pi}{6f_{vr}}} - \sqrt{\frac{2}{3}}\right)} \ln\left(\frac{\sqrt{2}\delta}{r_0}\right) \quad (8)$$

where $A(=0.85Gb/[2\pi(1-\nu)^{0.5}])$ is a constant, δ(≈6 nm) is the diameter of the rod-like η' precipitates (Fig. 9), f_{vr} is the volume fraction of the precipitates, and r_0(≈6 Å) is the radius of dislocation core [45]. The constant A is calculated to be 1.38×10^{-6} MPa·m, yielding the strengthening contribution from η' to be ~116 MPa.

According to Eq. (2), the accumulative strengthening effects of the alloy can be calculated. For the solid solutioned sample, the strengthening effects are mainly originated from the lattice friction stress, solid solution strengthening, dislocations, and Al_3Zr particles, considering the very large grain size (Fig. 2) and weak natural aging effect (the tensile tests were performed immediately after solid solution treatment). The YS of the solid solutioned sample is estimated to be 116 MPa, which is close to the measured result of (98±10) MPa. For the 8 P sample, the strengthening contribution is mainly originated from lattice friction stress, dislocations, grain boundaries, and Al_3Zr particles. The natural aging effect can be very weak for several reasons. First, the strengthening effect of natural aging can be less significant than other strengthening mechanisms. As indicated in Ref. [38], the YS of a 7075 aluminum alloy is improved from 583 to 658 MPa after one week of natural aging. Meanwhile, the tensile tests were performed after a very short time of the solid solution treatment (<36 h). Furthermore, the present alloy has a very low level of Mg content (0.7 wt.%), severely limiting the strengthening contribution from natural aging.

The strengthening contributions from different strengthening resources of the 8 P and aged 8 P sample are compared with the measured YS in Fig. 10. The calculated strengthening effects show an acceptable match with the measured YS: σ of the 8 P sample reaches 391 MPa, compared with the measured YS of (390±7) MPa; while σ of the aged 8 P sample is determined to be 379 MPa, compared with the measured YS of (405±9) MPa. Even though the 8 P sample shows very similar YS before and after aging, its strength is the result caused by the balance between the emerging new strengthening mechanism (precipitation hardening of η' phase) and the weakening of preexisting strengthening effects (grain boundary strengthening

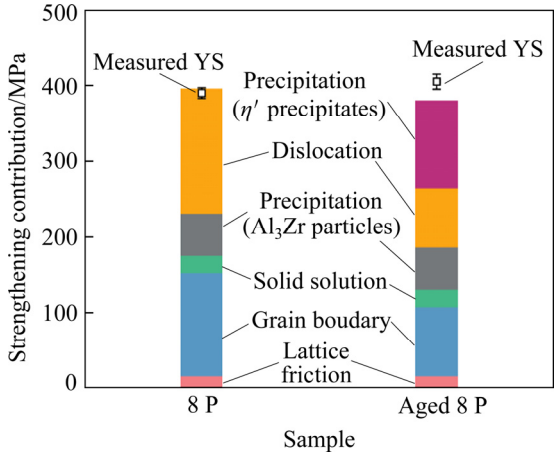

Fig. 10 Strengthening contribution from different mechanisms and comparison between 8 P sample before and after aging

and dislocations strengthening). As shown previously, the newly precipitated η' phases have contribution of ~116 MPa to the total strength. The following heat treatment, however, largely promotes the activity of dislocation motion, thus inducing dislocation annihilation and recrystallization [22]. The average grain size of the 8 P sample is increased from ~0.77 to ~1.7 μm, decreasing the grain boundary strengthening from ~136 to ~92 MPa. While the dislocation density of the 8 P sample is also decreased from ~5.8×10^{14} to ~1.3×10^{14} m^{-2} after aging, the corresponding strengthening contribution is decreased from ~136 to ~92 MPa.

4 Conclusions

(1) ECAP can effectively improve the strength and maintain high levels of ductility of the Al−Zn−Mg−Zr alloy. After 8 ECAP passes, the YS and UTS of the solid-solutioned sample are improved from (98±10) and (226±7) MPa to (390±7) and (430±5) MPa, respectively, with a high level of elongation ((16±2.2)%). The following aging slightly improves the YS and elongation of the 8 P sample to (405±9) MPa and (17.4±2.5)%, respectively, while the UTS remains at a similar level of (427±9) MPa.

(2) The repetitive ECAP can not only induce massive shear bands and dislocation entanglements but also promote the shear band collision and dislocation activity. Eight ECAP passes produce an ultrafine grain structure (with an average grain size of ~0.77 μm) consisting of ultrafine equiaxed grains and lath-like grains.

(3) The dislocation density can be improved significantly by ECAP pass. After a single ECAP pass, the dislocation density of the solid-solutioned sample soars from ~1.1×10^{13} to ~1.73×10^{14} m^{-2}. The dislocation density can be increased with ECAP pass and a very high value of ~5.8×10^{14} m^{-2} is achieved after 8 ECAP passes.

(4) The aging treatment on the 8 P sample can not only precipitate rod-like η' phases but also lead to the slight growth of grain size (from ~0.77 to ~1.70 μm) and decrease of dislocation density (from ~5.8×10^{14} to ~1.3×10^{14} m^{-2}).

(5) Even though the 8 P and aged 8 P sample show similar strength, the strengthening effects are different. The lattice friction, solid solution, and precipitation of Al_3Zr particles have contributions of 16, 23, and 55 MPa to both samples, respectively. The aging reduces strength contribution from grain boundaries (from ~136 to ~92 MPa), and dislocations (from ~161 to ~77 MPa). It, however, induces the precipitation of η' phase, which contributes to a strength increment of ~116 MPa.

Acknowledgments

This work was financially supported by the National Key Research and Development Plan, China (No. 2021YFC1910500).

References

[1] ZHU S, SHIH H C, CUI X, YU C Y, RINGER S P. Design of solute clustering during thermo-mechanical processing of AA6016 Al−Mg−Si alloy [J]. Acta Materialia, 2021, 203: 116455.

[2] CHEN Y, LIU C Y, ZHANG B, QIN F C, HOU Y F. Precipitation behavior and mechanical properties of Al−Zn−Mg alloy with high Zn concentration [J]. Journal of Alloys and Compounds, 2020, 825: 154005.

[3] LI Y, XU G F, LIU S C, WANG B F, PENG X Y. Study on anisotropy of Al−Zn−Mg−Sc−Zr alloy sheet [J]. Materials Characterization, 2021, 172: 110904.

[4] LI Y, XU G F, PENG X Y, WANG F X, DENG Y, LIANG X P. Effect of different aging treatment on high temperature properties of die-forged Al−5.87Zn−2.07Mg−2.42Cu alloy [J]. Materials Characterization, 2020, 164: 110239.

[5] PENG X Y, GUO Q, LIANG X P, DENG Y, GU Y, XU G F, YIN Z M. Mechanical properties, corrosion behavior and micro- structures of a non-isothermal ageing treated Al−Zn−Mg−Cu alloy [J]. Materials Science and Engineering A, 2017, 688: 146−154.

[6] ESMAEILI S, LLOYD D J, POOLE W J. A yield strength model for the Al−Mg−Si−Cu alloy AA6111 [J]. Acta Materialia, 2003, 51(8): 2243−2257.

[7] SENKOV O N, SHAGIEV M R, SENKOVA S V., MIRACLE D B. Precipitation of Al_3(Sc,Zr) particles in an Al−Zn−Mg−Cu−Sc−Zr alloy during conventional solution heat treatment and its effect on tensile properties [J]. Acta Materialia, 2008, 56: 3723−3738.

[8] HOLROYD N J H, BURNETT T L, SEIFI M, LEWANDOWSKI J J. Pre-exposure embrittlement of a commercial Al−Mg−Mn alloy, AA5083-H131 [J]. Corrosion Reviews, 2017, 35(4/5): 275−290.

[9] EL-MENSHAWY K, EL-SAYED A W A, EL-BEDAWY M E, AHMED H A, EL-RAGHY S M. Effect of aging time at low aging temperatures on the corrosion of aluminum alloy 6061 [J]. Corrosion Science, 2012, 54(1): 167−173.

[10] HE L Z, CHEN Y B, CUI J Z, SUN X F, GUAN H R, HU Z Q. Effect of Cu content on intergranular corrosion of a new type Al−Mg−Si alloy [J]. Corrosion Science and Protection Technology, 2004, 16: 129−133.

[11] CHEN X, HUANG G S, LIU S S, HAN T Z, JIANG B,

TANG A T, ZHU Y T, PAN F S. Grain refinement and mechanical properties of pure aluminum processed by accumulative extrusion bonding [J]. Transactions of Nonferrous Metals Society of China, 2019, 29(3): 437−447.

[12] KHODABAKHSHI A R, KAZEMINEZHAD M. Effects of non-isothermal annealing on microstructure and mechanical properties of severely deformed aluminum samples: Modeling and experiment [J]. Transactions of Nonferrous Metals Society of China, 2019, 29(6): 1127−1137.

[13] BAKHSHI R, FARSHIDI M H, SAJJADI S A. Strengthening of aluminium alloy 7005 through imposition of severe plastic deformation supplemented by different ageing treatments [J]. Transactions of Nonferrous Metals Society of China, 2021, 31(10): 2909−2921.

[14] TANG L, PENG X Y, HUANG J W, MA A B, DENG Y, XU G F. Microstructure and mechanical properties of severely deformed Al−Mg−Sc−Zr alloy and their evolution during annealing [J]. Materials Science and Engineering A, 2019, 754: 295−308.

[15] GONZÁLEZ-MASÍS J, CUBERO-SESIN J M, CAMPOS-QUIRÓS A, EDALATI K. Synthesis of biocompatible high-entropy alloy TiNbZrTaHf by high-pressure torsion [J]. Materials Science and Engineering A, 2021, 825: 141869.

[16] JIANG S, PENG R L, HEGEDŰS Z, GNÄUPEL-HEROLD T, MOVERARE J J, LIENERT U, FANG F, ZHAO X, ZUO L, JIA N. Micromechanical behavior of multilayered Ti/Nb composites processed by accumulative roll bonding: An in-situ synchrotron X-ray diffraction investigation [J]. Acta Materialia, 2021, 205: 116546.

[17] MESHKABADI R, FARAJI G, JAVDANI A, POUYAFAR V. Combined effects of ECAP and subsequent heating parameters on semi-solid microstructure of 7075 aluminum alloy [J]. Transactions of Nonferrous Metals Society of China, 2016, 26(12): 3091−3101.

[18] SHAERI M H, SHAERI M, SALEHI M T, SEYYEDEIN S H, DJAVANROODI F. Microstructure and texture evolution of Al-7075 alloy processed by equal channel angular pressing [J]. Transactions of Nonferrous Metals Society of China, 2015, 25(5): 1367−1375.

[19] ZHA M, LI Y, MATHIESEN R H, BJØRGE R, ROVEN H J. Microstructure evolution and mechanical behavior of a binary Al−7Mg alloy processed by equal-channel angular pressing [J]. Acta Materialia, 2015, 84: 42−54.

[20] ZHAO Y H, LIAO X Z, JIN Z, VALIEV R Z, ZHU Y T. Microstructures and mechanical properties of ultrafine grained 7075 Al alloy processed by ECAP and their evolutions during annealing [J]. Acta Materialia, 2004, 52: 4589−4599.

[21] TANG L, WANG L, WANG M S, LIU H B, KABRA S, CHIU Y, CAI B. Synergistic deformation pathways in a TWIP steel at cryogenic temperatures: In situ neutron diffraction [J]. Acta Materialia, 2020, 200: 943−958.

[22] DUAN Y L, TANG L, XU G F, DENG Y, YIN Z M. Microstructure and mechanical properties of 7005 aluminum alloy processed by room temperature ECAP and subsequent annealing [J]. Journal of Alloys and Compounds, 2016, 664: 518−529.

[23] NIE Y, CLAUS B, GAO J, ZHAI X, KEDIR N, CHU J, SUN T, FEZZAA K, CHEN W W. In situ observation of adiabatic shear band formation in aluminum alloys [J]. Experimental Mechanics, 2020, 60(2): 153−163.

[24] ALMASRI A H. Dynamic shear bands in metals under high strain rates [D]. Louisiana State University, Baton Rouge, 2008.

[25] ROBSON J D, PRANGNELL P B. Dispersoid precipitation and process modelling in zirconium containing commercial aluminium alloys [J]. Acta Materialia, 2001, 49: 599−613.

[26] UNGÁR T, BORBÉLY A. The effect of dislocation contrast on X-ray line broadening: A new approach to line profile analysis [J]. Applied Physics Letters, 1996, 69(21): 3173−3175.

[27] SIMM T H, WITHERS P J, QUINTA DA FONSECA J. An evaluation of diffraction peak profile analysis (DPPA) methods to study plastically deformed metals [J]. Materials and Design, 2016, 111: 331−343.

[28] LEE T H, SHIN E, OH C S, HA H Y, KIM S J. Correlation between stacking fault energy and deformation microstructure in high-interstitial-alloyed austenitic steels [J]. Acta Materialia, 2010, 58: 3173−3186.

[29] JIANG F Q, TANG L, HUANG J W, CAI Y H, YIN Z M. Influence of equal channel angular pressing on the evolution of microstructures, aging behavior and mechanical properties of as-quenched Al−6.6Zn−1.25Mg alloy [J]. Materials Characterization, 2019, 153: 1−13.

[30] IWAHASHI Y, WANG J, HORITA Z, NEMOTO M, LANGDON T G. Principle of equal-channel angular pressing for the processing of ultra-fine grained materials [J]. Scripta Materialia, 1996, 35: 143−146.

[31] KENDIG K L, MIRACLE D B. Strengthening mechanisms of an Al−Mg−Sc−Zr alloy [J]. Acta Materialia, 2002, 50: 4165−4175.

[32] KHALFALLAH A, RAHO A A, AMZERT S, DJEMLI A. Precipitation kinetics of GP zones, metastable η' phase and equilibrium η phase in Al−5.46wt.%Zn−1.67wt.%Mg alloy [J]. Transactions of Nonferrous Metals Society of China, 2019, 29(2): 233−241.

[33] LIU J Z, CHEN J H, YANG X B, REN S, WU C L, XU H Y, ZOU J. Revisiting the precipitation sequence in Al−Zn−Mg-based alloys by high-resolution transmission electron microscopy [J]. Scripta Materialia, 2010, 63: 1061−1064.

[34] ZHAO Y H, LIAO X Z, JIN Z, VALIEV R Z, ZHU Y T. Microstructures and mechanical properties of ultrafine grained 7075 Al alloy processed by ECAP and their evolutions during annealing [J]. Acta Materialia, 2004, 52: 4589−4599.

[35] SHA G, CEREZO A. Early-stage precipitation in Al−Zn−Mg−Cu alloy (7050) [J]. Acta Materialia, 2004, 52: 4503−4516.

[36] ZHANG S, HU W, BERGHAMMER R, GOTTSTEIN G. Microstructure evolution and deformation behavior of ultrafine-grained Al−Zn−Mg alloys with fine η' precipitates [J]. Acta Materialia, 2010, 58: 6695−6705.

[37] HORNBOGEN E, STARKE E A. Overview No. 102: Theory assisted design of high strength low alloy aluminum [J]. Acta Metallurgica et Materialia, 1993, 41: 1−16.

[38] MA K, WEN H, HU T, TOPPING T D, ISHEIM D, SEIDMAN D N, LAVERNIA E J, SCHOENUNG J M. Mechanical behavior and strengthening mechanisms in

ultrafine grain precipitation-strengthened aluminum alloy [J]. Acta Materialia, 2014, 62: 141−155.

[39] BALOGH L, UNGÁR T, ZHAO Y, ZHU Y T, HORITA Z, XU C, LANGDON T G. Influence of stacking-fault energy on microstructural characteristics of ultrafine-grain copper and copper–zinc alloys [J]. Acta Materialia, 2008, 56: 809−820.

[40] XIAO Q F, HUANG J W, JIANG Y G, JIANG F Q, WU Y F, XU G F. Effects of minor Sc and Zr additions on mechanical properties and microstructure evolution of Al−Zn−Mg−Cu alloys [J]. Transactions of Nonferrous Metals Society of China, 2020, 30(6): 1429−1438.

[41] FULLER C B, SEIDMAN D N, DUNAND D C. Mechanical properties of Al(Sc,Zr) alloys at ambient and elevated temperatures [J]. Acta Materialia, 2003, 51: 4803−4814.

[42] SEIDMAN D N, MARQUIS E A, DUNAND D C. Precipitation strengthening at ambient and elevated temperatures of heat-treatable Al(Sc) alloys [J]. Acta Materialia, 2002, 50: 4021−4035.

[43] XIE Y P, WANG Z Y, HOU Z F. The phase stability and elastic properties of $MgZn_2$ and Mg_4Zn_7 in Mg−Zn alloys [J]. Scripta Materialia, 2013, 68: 495−498.

[44] CHOI S, JEON J, SEO N, SON S B, LEE S J. Effect of heating rate on microstructure and mechanical properties in Al 7055 [J]. Metals and Materials International, 2021, 27(3): 449−455.

[45] XUE H, YANG C, KUANG J, ZHANG P, ZHANG J Y, LIU G, SUN J. Highly interdependent dual precipitation and its effect on mechanical properties of Al−Cu−Sc alloys [J]. Materials Science and Engineering A, 2021, 820: 141526.

通过等通道转角挤压及后续时效制备高强韧 Al−Zn−Mg−Zr 合金

唐 磊[1]，彭小燕[2,3]，江福清[4]，李 耀[2]，徐国富[2,3]

1. School of Metallurgy and Materials, University of Birmingham, B15 2TT, United Kingdom；
2. 中南大学 材料科学与工程学院，长沙 410083；
3. 中南大学 有色金属材料科学与工程教育部重点实验室，长沙 410083；
4. 中国科学院 金属研究所，沈阳 110016

摘 要：通过多道次等通道转角挤压(ECAP)及后续时效制备具有超细晶结构的高强韧 Al−Zn−Mg−Zr 合金。在经过 8 道次 ECAP 和后续时效后，固溶态合金的屈服强度和抗拉强度分别由(98±10) MPa 和(226±7) MPa 显著提升到(405±7) MPa 和(427±9) MPa，同时合金能保持较好的伸长率((17.4±2.5)%)。采用多尺度表征手段(透射电镜、背散射电子衍射和 X 射线衍射)揭示合金的微观结构(包括晶粒细化、析出相形貌和位错密度)在 ECAP 和后续时效中的演变。经过 8 道次 ECAP 后，原本粗大的长晶粒被细化成独特的双晶粒结构(由极细等轴晶和条状晶粒组成)。同时，具体讨论一系列强化效应(例如：位错强化和析出强化)在 ECAP 和后续时效中的作用。

关键词：等通道转角挤压；Al−Zn−Mg−Zr 合金；晶粒细化；强化机制

(Edited by Bing YANG)